

## Accepted Manuscript

Improvement of mechanical strength of hydrophobic coating on glass surfaces by an atmospheric pressure plasma jet

Md. Mokter Hossain, Quang Hung Trinh, M.S.P. Sudhakaran, Lamia Sultana, Young Sun Mok



PII: S0257-8972(18)31056-9  
DOI: doi:[10.1016/j.surfcoat.2018.09.071](https://doi.org/10.1016/j.surfcoat.2018.09.071)  
Reference: SCT 23845  
To appear in: *Surface & Coatings Technology*  
Received date: 23 November 2017  
Revised date: 22 July 2018  
Accepted date: 12 September 2018

Please cite this article as: Md. Mokter Hossain, Quang Hung Trinh, M.S.P. Sudhakaran, Lamia Sultana, Young Sun Mok , Improvement of mechanical strength of hydrophobic coating on glass surfaces by an atmospheric pressure plasma jet. Sct (2018), doi:[10.1016/j.surfcoat.2018.09.071](https://doi.org/10.1016/j.surfcoat.2018.09.071)

This is a PDF file of an unedited manuscript that has been accepted for publication. As a service to our customers we are providing this early version of the manuscript. The manuscript will undergo copyediting, typesetting, and review of the resulting proof before it is published in its final form. Please note that during the production process errors may be discovered which could affect the content, and all legal disclaimers that apply to the journal pertain.

# Improvement of mechanical strength of hydrophobic coating on glass surfaces by an atmospheric pressure plasma jet

Md. Mokter Hossain<sup>a</sup>, Quang Hung Trinh<sup>b,c</sup>, M.S.P. Sudhakaran<sup>a</sup>, Lamia Sultana<sup>a</sup>, Young Sun Mok<sup>a,\*</sup>

<sup>a</sup>Department of Chemical and Biological Engineering, Jeju National University, Jeju 63243, Korea

<sup>b</sup>Institute of Research and Development, Duy Tan University, Da Nang 550000, Vietnam

<sup>c</sup>Faculty of Mechanical Engineering, Le Quy Don Technical University, 236 Hoang Quoc Viet, Hanoi, Vietnam

\*Corresponding author, Tel: (+82)64-754-3680, Fax: (+82)64-755-3670, E-mail: smokie@jejunu.ac.kr

Abstract: Non-thermal plasma is getting more popular in industrial applications, mainly treatment of material surfaces. Hydrophobic coatings often suffer mechanical instability and do not function well after abrasion/scratching. In this study, non-thermal plasma jet generated at atmospheric pressure in ambient condition was applied to the hydrophobic treatment of glass surface using two precursors. Tetramethylsilane (TMS) was used to promote hydrophobicity and (3-Aminopropyl)triethoxysilane (APTES) was used to get durable mechanical strength of the coating although it is hydrophilic in character. An alternating current (AC) high voltage (operating frequency: 11.5 kHz) was used to generate plasma jet for producing a coating layer onto the soda-lime glass sample. Water contact angle of 139° and a stable mechanical strength were achieved at an optimal TMS/APTES ratio of 4.8. The coating thickness, strength and water contact angle were varied by changing treatment time, applied voltage, and carrier gas (argon) flow rate. The coating layer were characterized by atomic-force microscopy (AFM), scanning electron microscope (SEM), X-ray photoelectron spectroscopy (XPS), Fourier transform infrared spectroscopy (FTIR), water contact angle (WCA), scratch test and UV/visible spectroscopy.

Keywords: non-thermal plasma, atmospheric pressure plasma jet, hydrophobic coating

## 1. Introduction

Making hydrophobic surface of various materials by nonthermal plasma (NTP) treatment at atmospheric pressure has been a warm research topic in recent years [1–7]. Researchers found the idea to make hydrophobic surface from nature [8–10] to use it for various purposes such as self-cleaning windows, ultra-dry surface applications, self-cleaning of antennas, anti-icing, out-door textiles, protection of circuits and grids, medical devices and other optical apparatuses [11–15]. In order to obtain hydrophobic characteristics the surface requires nano-scale and micro-scale roughness which can be done by applying low surface energy coating. Basically, the surface roughness and the surface chemistry both affect the hydrophobicity [16]. The hydrophobic coating can be done by plasma treatment, by deep coating or by spraying low surface energy materials on the surface. The surface having water contact angle (WCA)  $< 90^\circ$  is known as hydrophilic surface but having WCA  $\geq 90^\circ$  is known as hydrophobic surface. On the other hand, surface having WCA  $> 150^\circ$  and sliding angle (SA)  $\leq 10^\circ$  is called super-hydrophobic surface due to its excellent self-cleaning ability. Generally, WCA and SA indicate the performance of the surface how much it will be effective in self-cleaning function.

The major drawback of the coatings is its poor mechanical abrasion which extinguishes the self-cleaning function due to the damage of roughness and coating layer. As a result, for this experiment two different precursors have been selected to investigate the mechanical strength of the coating. Tetramethylsilane (TMS,  $\text{Si}(\text{CH}_3)_4$ ) used to promote hydrophobicity in this work is an organosilicon compound precursor having the formula  $\text{Si}(\text{CH}_3)_4$ . Though TMS is a good promoter of hydrophobicity, due to its poor adhesion to metal or inorganic material, the coating does not survive for longtime. To overcome this problem an additive precursor called (3-Aminopropyl)triethoxysilane (APTES,  $\text{H}_2\text{N}(\text{CH}_2)_3\text{Si}(\text{OC}_2\text{H}_5)_3$ ) is also used together with TMS to make robust coating on the glass surface. APTES is an aminosilane basically used in the process

of silanization as well as the functionalization of surfaces with alkoxy silane molecules. In recent times, APTES is highly recommended to use for surface coating due to its covalent attaching of organic films to metal oxides, silica ( $\text{SiO}_2$ ) [16] and titania ( $\text{TiO}_2$ ). Masuko et al. [17] studied the shear strength and durability of self-assembled monolayer (SAM) and the tribology performance with different numbers of siloxane bonds on smooth silicon substrates. They showed that increasing the number of siloxane bonds with SAMs actually allows the stable low friction and greater durability. Therefore, APTES having these advantages is selected as a promoter for robust coating to improve the wear resistance of the surface although it is hydrophilic in character.

Nowadays, NTPs are very popular to create a thin film polymer layer onto different surfaces such as silicon, glass, wood, and fabric. The pioneer advantage of the NTP is that polymerization or deposition for the coating can be easily controlled by controlling electric power and gas flow rate. Topala et al. [18] used DBD plasma to deposit thin film onto glass and silicon substrates to get stable hydrophobic surface. With these background knowledges, non-thermal plasma jet operating at atmospheric pressure has been selected for this work. One of the key parameters explored was the ratio of TMS to APTES.

## 2. Experimental

Figure 1 shows the schematic figure of the experimental setup and custom-built scratch tester and Figure 2 shows the discharge image of the plasma jet. The plasma jet was composed of a glass tube having a coaxially inserted stainless steel rod with a sharp tip acting as the high voltage (HV) electrode. The orifice of the glass tube from which the plasma jet was discharged had the inner and outer diameters of 5.0 and 8.0 mm, respectively. The HV electrode was connected to an AC power source purchased from Korea Switching Co., which could deliver maximum 7.5 kV at an operating frequency of 11.5 kHz. The distance between the tip of the HV

electrode and the end of the tube and the gap from the end of the tube to the substrate were kept constant at 75 and 2 mm, respectively. Argon gas (99.99%) was used as a main carrier gas at a rate of 1600 cm<sup>3</sup> min<sup>-1</sup> (sccm). TMS (Sigma-Aldrich Korea Co., Ltd) was used to promote hydrophobicity, and APTES (Sigma-Aldrich Korea Co., Ltd) was used to promote the robustness of the coating. The precursors were delivered to the jet by bubbling liquid TMS and APTES (at 20 and 121°C, respectively) contained in pyrex flasks using Ar gas. All Ar flows were precisely controlled by mass flow controllers (MFCs). The TMS/APTES ratio was varied from 3.0 to 6.0 to investigate its effect on the thin film obtained by the plasma polymerization. The TMS concentration was changed by the feed gas from 4304 ppm (parts per million, volumetric) to 8450 ppm, while APTES concentration was kept constant at 1408 ppm. The main carrier gas and precursor mixture were separately fed into the jet. The substrate for the coating was soda-lime glass with a dimension of 75 mm × 27 mm × 1.2 mm. For simplicity, the substrates were set to stand still during coating. The resulting coated area was estimated to be about 20 mm<sup>2</sup>.

It is important to know the WCA of the coated surface for understanding the character of the coated surface polymer. The WCA measurements were carried out on a goniometer (Phonix 300, Surface & Electro Optics Co., Ltd., Korea) using sessile drop technique by dropping about 10 μL of distilled water. To see the surface nanostructures of the coating, atomic force microscopy (AFM, Nano Xpert II, EM4SYS, USA) was performed. The surface morphology was observed by scanning electron microscopy (SEM, JSM-6700F, JEOL, Japan) at an operating voltage of 15kV. The coating surface chemistry was analyzed using an X-ray photoelectron spectroscopy (XPS). A Fourier transform infrared spectroscopy (FTIR, FTIR-7600, Lambda Scientific, Australia) was used to investigate the composition of the effluent from the plasma jet and the deposited thin films. Measurement of mechanical strength of the coating was carried out using a custom-built scratch tester and the wear tracks were observed by an optical microscope

(2MP 1000X 8 LED USB Digital Microscope Endoscope Zoom Camera, A4Tech, Taiwan). Many researchers used scratch test to assess the coating adhesion and robustness [19–26]. A new scratch test methodology was recently developed to use in various modes of scratch test to quantify scratch resistance of polymeric coatings [27]. Richard et al. [28] used combination of scratch test and acoustic microscopy imaging for the study of coating adhesion. Scratch test is a simple and rapid method for characterizing the coatings. Obtained results by scratch test are influenced by various factor such as coating thickness, interfacial bond strength, mechanical properties of substrate, test condition such as load, scratch speed, and indenter tip radius [29]. Scratch testing is usually performed by moving sharp tip on the coated surface with either constant or progressively increasing load to create a scratch [30]. The scratch tester used in this work is shown in Figure 1(b). Its main parts include a dc motor, a needle holder, a needle, a sliding guidance, and a control panel. An iron needle having a tip with a diameter of 0.5 mm was used. Yarn was used to connect the driving shaft of the motor to the needle holder. The needle holder was guided by the sliding guidance so that it can move horizontally back and forth. The moving speed of the needle was set to 37 mm/s. A sample for testing was put under the needle and fixed by using double sided tape. For each measurement, the tip of the needle was cleaned with acetone and tissue wiper.

### **3. Results and discussion**

#### **3.1. Hydrophobic treatment of glass and water contact angle measurement**

The hydrophobic treatment by the plasma polymerization process depended on a number of parameters such as applied voltage, treatment time, the TMS/APTES ratio and the gas flow rate. At first, the effect of the treatment time was examined from 30 s to 420 s at a TMS/APTES ratio of 4.8 and an applied voltage of 7.5 kV., and then the effect of the applied voltage,

TMS/APTES ratio and the gas flow rate on the coating was examined one by one with the other parameters kept constant. Figure 3 shows the dependence of WCA on the treatment time, the applied voltage, the TMS/APTES ratio and the feed gas flow rate. As seen in Fig. 3 (a), the WCA significantly increased from  $87^\circ$  to  $139^\circ$  with increasing the treatment time up to 300 s and seemed to level off thereafter. The improvement of the coating in terms of WCA is related to the surface coverage which increased with increasing the treatment time.

Second step was to find out appropriate applied voltage and hence the TMS/APTES ratio and treatment time were kept constant at 4.8 and 300 s, respectively. As shown in Fig. 3(b), a similar increasing trend in the WCA was observed. The higher the applied voltage, the more intense the plasma was, leading to the enhancement in the deposition rate and the formation of particulates in the plasma gas phase, called dusty plasma. The high surface roughness and therefore the high WCA of the coating is strongly related to the deposition of the formed particulates on the substrate. At the applied voltage of 7.5 kV, the WCA was observed to be ca.  $139^\circ$ . The surface roughness of the obtained coatings will be discussed below.

After having an idea of treatment time and applied voltage the TMS/APTES ratio was varied while the treatment time and applied voltage were kept constant at 300 s and 7.5 kV, respectively. Figure 3(c) shows the dependence of WCA on the TMS/APTES ratio. The WCA values of the coatings formed from the single precursor of APTES and TMS are also added for the purpose of comparison. It is natural that the WCA should increase with increasing the TMS/APTES ratio due to the hydrophobic character of TMS. At the TMS/APTES ratio of 6, the WCA shows the similar values achieved by the TMS-alone coating. Further, increase the ratio only increase the thickness but WCA angle remain same like as the TMS/APTES ratio of 6. Meanwhile, the low WCA of the APTES-alone coating clearly showed the hydrophilic nature of APTES.

Finally, we changed the flow rate of the gas to see the effect of the WCA while treatment time, applied voltage, the TMS/APTES ratio were kept constant at 300 s, 7.5 kV, and 4.8 respectively. Figure 3(d) shows the result of the flow rate change from 1000 sccm to 1600 sccm. It was observed that the plasma was getting more intense, leading to an increased WCA from 123° to 139°. But further increases of the feed gas flow rate to 2000 sccm slightly decreased the WCA to 136°, and hence 1600 sccm was chosen for the optimal gas flow rate.

Figure 4 displays the photographic images of the water droplet on various substrates in the coated state. Here, top view was added to see the surface of the coating and side view to see the WCA.

### 3.2. Coating stability

For this work, the plasma-treated samples were stored in centrifuge tube at room temperature to check the coating stability under the effect of natural aging and thermal heating. Aging time has a great effect on WCA for the powder substrate coating [31]. For powder substrate coating, WCA can increase by 15° to 40° within 30 days [31]. Figure 5(a) shows the effect of aging (15 days and 30 days) on WCA, where it can be easily understood that there is negligible aging effect on WCA. In other words, the coating is stable and durable. The thermal stability of the coating was examined by annealing tests at 200 °C and 250 °C for one hour. In both cases, there was no change in WCA, as shown in Figure 5(b).

### 3.3. Coating thickness and surface morphology

The AFM and SEM analyses were performed to examine the effect of TMS/APTES ratio on the surface morphology and surface roughness of the coatings. Figure 6 shows the AFM results of the coated samples with various TMS/APTES ratios. The corresponding root-mean-

squared (RMS) roughness and coating thickness values are listed in Table 1. As seen, the morphologies of all coatings were similar regardless of the precursor ratio, displaying rough and needle-like surfaces. However, the RMS roughness seemed to increase with increasing the TMS/APTES ratio, which is consistent with the increased WCA. Among the coated samples, the APTES-alone case showed the lowest surface roughness. Meanwhile, the opposite was true for the TMS-alone case. The formation of rough surfaces with nanoscale topographic features results from the generation of particulates through gas-phase condensation reactions. The plasma-induced particulates are then deposited and adhere to a substrate [5]. In plasma, TMS seemed to be more active than APTES to produce more fragments, facilitating the formation of particulates and therefore the high surface roughness.

The SEM images of the corresponding samples are shown in Figure 7. The coatings consist of nanostructures ranging from 70 to 250 nm. It is clear that at high TMS/APTES ratios, the particulates were intensively formed and deposited on the substrates. It is found that the coatings have shown cauliflower morphology in the case of TMS-alone and the TMS/APTES ratio of 6 (Figure 7(g) and Figure 7(f), respectively) but in other cases the nanostructures like circular island with different sizes were formed. In comparison, at low TMS/APTES ratios, the particulates adhered to smooth layers that were mainly formed from APTES.

### **3.4. Gas-phase FTIR analysis**

#### **3.4.1. Gas-phase analysis of the effluent of the Ar/TMS plasma**

Figure 8 shows the FTIR spectra of the Ar/TMS and Ar/APTES mixture without (black) and with (red) plasma ignition. If we look at the figure (Figure 8(a) & Figure 8(b)), the main significant difference is the reduction of IR peak intensities in the case of plasma turned on due to the TMS and APTES decomposition. When the plasma is turned on, the absorption intensities for

both TMS and APTES decreased which indicates that these precursors compounds were decomposed by plasma. Figure 8(a) presents the infrared spectra for the gas-phase effluent of the Ar/TMS mixture. Strong peaks were observed from  $1000\text{ cm}^{-1}$  to  $1500\text{ cm}^{-1}$  and from  $2800\text{ cm}^{-1}$  to  $3300\text{ cm}^{-1}$ , while some other weak peaks appeared at wavenumbers from  $1800\text{ cm}^{-1}$  to  $2400\text{ cm}^{-1}$  (see the insets). Here, the peaks at  $1256\text{ cm}^{-1}$ ,  $1289\text{ cm}^{-1}$ ,  $1430\text{ cm}^{-1}$ ,  $2823\text{ cm}^{-1}$ , and  $2965\text{ cm}^{-1}$  are due to TMS [32–34]. The strong deformation of  $\text{CH}_3$  symmetric groups are found at  $1247\text{ cm}^{-1}$  and  $1265\text{ cm}^{-1}$  [34]. A weak SiO peak at  $1065\text{ cm}^{-1}$  is found only in Ar/TMS with plasma.  $\text{CH}_3$  rock,  $\text{SiH}_2$  bend, and Si-H symmetric stretching are observed at  $3050\text{--}3100\text{ cm}^{-1}$  only in Ar/TMS without plasma [33–35]. The infrared spectra also detected the very weak peak of  $\text{CO}_2$  at  $2350\text{ cm}^{-1}$ , Si-H stretching at  $2129\text{ cm}^{-1}$ , and deformation of  $\text{CH}_3$  symmetric groups at  $1863\text{ cm}^{-1}$  and  $1947\text{ cm}^{-1}$  [33–35].

### 3.4.2. Gas-phase analysis of the effluent of Ar/APTES plasma

The gas-phase FTIR spectra of the Ar/APTES mixture without (black) and with (red) plasma ignition are shown in Figure 8(b). A high-intensity peak at  $1065\text{ cm}^{-1}$  is assigned to the vibration of Si-O in APTES [35–37]. A strong asymmetric peak at  $1242\text{ cm}^{-1}$  is due to the vibration of SiO- $\text{CH}_2$  [35]. Weak peaks at  $1451\text{ cm}^{-1}$  and  $1475\text{ cm}^{-1}$  are attributed to H-C-H bends, while the strong peak at  $1395\text{ cm}^{-1}$  is for the  $\text{CH}_2$  bending. The H-C-H bending at  $1475\text{ cm}^{-1}$  is only found in Ar/APTES mixture without plasma [36,38,39]. The Strong asymmetric peak at  $2903\text{ cm}^{-1}$  and very strong symmetric peak at  $2985\text{ cm}^{-1}$  are found for the vibration of  $\text{CH}_2$  [35]. Very weak O-H stretch mode of Si-OH- $\text{NH}_2$  group is detected at the frequency of  $2762\text{ cm}^{-1}$ , which is only observed in the Ar/APTES mixture with plasma [40]. The infrared spectra also detected C=O bend at  $1746\text{ cm}^{-1}$  and CO at  $2140\text{ cm}^{-1}$  only in Ar/APTES with plasma case. A

weak peak appearing at  $1923\text{ cm}^{-1}$  may be ascribed to  $\text{SiO}+\text{CH}_3$  bend in both with and without plasma [35,37].

To see the effect of gas phase on the hydrophobicity, one more experiment was done using TMS/APTES mixture without plasma discharge, and then the WCA of the glass was measured. It has shown there was no change in hydrophobicity under such a condition.

### 3.4.3. Possible reaction routes and mechanism of APTES for the surface modification

Siloxane-based plasma polymerization with primary amines using a single amino-alkoxysilane precursor is still under investigation and only a few articles discussed about this issue [41–45]. The Plasma-assisted APTES polymerization is described in Figure 9 [46–48]. The process can be divided into three parts: (a) hydrogen bonding due to initial adsorption, (b) surface attachment, and (c) multilayer formation. The polymer surface by the hydrogen bonding is the 1<sup>st</sup> step (Figure 9(a)) of physical process of APTES [48] where siloxane bond formation by the ethoxy groups with neighbors H-bonded to the surface with free APTES molecules can be seen in Figure 9(b). From Figure 9(a) and 9(b) still there is no sign of donor amine and acceptor groups. This means that some of APTES molecules are not H-bonded to the surface. Basically, the inter-APTES reactions lead to the formation of siloxane cross-link and it makes a thin layer (Figure 9(c)) where donor amine and acceptor H-bond both are present.

### 3.5. FTIR analysis of the coating layer

So as to take the FTIR spectra of the coating layer, the coatings were prepared on infrared-transparent KBr discs instead of the glass substrates. Note that strong IR adsorption of glass hinders the infrared analysis of the coating layer. The obtained results are shown in Figure 10. The most intense peaks are seen in the region B in the range of 1010-1240  $\text{cm}^{-1}$ . These peaks are due to the Si-O stretching in Si-O-Si [49,50]. In the region A, the Si-C stretching is seen at 800  $\text{cm}^{-1}$  [49] and the peaks of Si-O stretching in Si-OH are seen at 830-940  $\text{cm}^{-1}$  [49-51]. In the regions C and F, the peaks at 1260  $\text{cm}^{-1}$  and 2970  $\text{cm}^{-1}$  are related to Si-CH<sub>3</sub> symmetric deformation and Si-CH<sub>2</sub> deformation or Si-CH<sub>3</sub> asymmetric stretching appears at 1410  $\text{cm}^{-1}$  [52,53]. The wide Si-OH stretching vibration is seen in the region F [49,54].

### 3.6. XPS analysis

The XPS analysis was carried out to identify the surface chemical composition of the coatings. From the XPS study, it was found that the uncoated soda-lime glass contains silicon (Si), carbon (C), calcium (Ca), nitrogen (N), oxygen (O) and sodium (Na). On the other hand, silicon (Si), carbon (C), nitrogen (N) and oxygen (O) were found in the coated glasses. Figure 11 shows the concentrations of the elements observed for the bare glass and the ones coated with only TMS, only APTES and TMS/APTES mixture of a ratio of 4.8. The plasma-treated glass with TMS alone did not contain any nitrogen in the coating layer. 35% carbon in the bare glass is probably due to the presence of adventitious carbon on the sample's surface [3]. The presence of carbon of the coated glasses was provided by both adventitious and precursors.

The deconvolution of C1s spectra is shown in Figure 12 and the peak positions of C1s with the corresponding functional groups are seen in Table 2. H-C or C-C peak was found at ~284.7 eV from all the samples [3,55]. The peak at around 286 eV also appeared from all the samples due to the C-O bond. The C-N group appeared from the APTES and TMS/APTES coated samples

(Figures 12(c) and 12(d)) [3,55]. The peak at  $\sim 287.5$  eV was due to C=O in the coated samples (Figures 12(b), 12(c), and 12(d)) and peak at  $\sim 288.7$  eV was found due to O-C-O in the uncoated sample and the ones coated with only APTES and TMS/APTES mixture [3,55].

### 3.7. UV-Vis transmission spectra result

Figure 13 shows the UV-Vis transmission spectra of the bare glass and the ones coated with APTES, TMS, and their mixture at various ratios. Transmittance and hydrophobicity both depend on the thickness and roughness of the coating. In order to increase the hydrophobic property, thickness and roughness need to be increased, however, the visibility has to be sacrificed [56]. The transparency of the coated glasses in the visible region (from 390 to 700 nm) decreased with increasing the TMS/APTES ratio. Bare glass exhibited around 80% transmittance in the visible regions, while the plasma-treated glasses at different TMS/APTES ratios showed transmittance from 80 to 65%.

### 3.8. Scratch test

For finding the same coating thickness, the deposition rate of each sample was calculated. Four samples with different treatment time for TMS/APTES=4.8 sample was generated. After that, the thickness of each sample was measured and plotted in Microsoft Excel and found the slope which was the deposition rate. By doing this, the deposition rate was calculated for each sample. After analyzing all the sample thickness, 400 nm thickness was considered for the scratch test. So each sample should have 400 nm thickness for scratch test. Scratch tests were conducted after annealing the samples at  $250^{\circ}$  C for 1 h. The minimum force applied to the needle tip was 3430 dyne, which was applied to all the samples. For the samples that could sustain the 3430 dyne force, the force was gradually increased to find the breakdown force. The

experimental conditions are summarized in Table 3. Figure 14 shows the results of the scratch tests, and Figure S1 shows the images of the scratch tests. As can be seen, the presence of APTES as a precursor greatly enhanced the scratch resistance of the coating layer, compared to the coating with only TMS. For example, the TMS coating was totally destroyed by the needle at the applied force of 3432 dyne. In comparison, at the same force, the TMS/APTES coating was only slightly scratched by the needle.

#### 4. Conclusions

The purpose of this work was to prepare a robust coating with good hydrophobic character as well as wear resistance by using non-thermal plasma jet with the mixture of two precursors. TMS was to promote hydrophobic character and APTES to increase the mechanical strength and durability owing to the presence of amines capable of promoting adhesion. The appropriate operating condition in terms of both hydrophobicity and mechanical strength was found to be the TMS/APTES ratio of 4.8, the applied voltage of 7.5 kV, and the treatment time of 300 s. At this condition, the WCA achieved was  $139^\circ$ . The aging and annealing tests have shown that the coating layer prepared on the glass is stable and durable. The AFM and SEM images indicated that the hydrophobic property of the coating is closely related to the thickness and roughness. According to the UV-Vis transmission spectra of the glass coated with the TMS and APTES mixture, there was no significant loss in the visibility. The non-thermal plasma jet operating at atmospheric pressure can be a promising candidate for the preparation of hydrophobic coating.

#### Acknowledgment

This work was supported by the 2017 Scientific Promotion Program funded by Jeju National University.

## References

- [1] J. Genzer, K. Efimenko, Recent developments in superhydrophobic surfaces and their relevance to marine fouling: a review, *Biofouling*. 22 (2006) 339–360.
- [2] X.-M. Li, D. Reinhoudt, M. Crego-Calama, What do we need for a superhydrophobic surface? A review on the recent progress in the preparation of superhydrophobic surfaces, *Chem. Soc. Rev.* 36 (2007) 1350.
- [3] R. Múgica-Vidal, F. Alba-Elías, E. Sainz-García, J. Ordieres-Meré, Atmospheric plasma-polymerization of hydrophobic and wear-resistant coatings on glass substrates, *Surf. Coatings Technol.* 259 (2014) 374–385.
- [4] J.H. Yim, V. Rodriguez-Santiago, A.A. Williams, T. Gougousi, D.D. Pappas, J.K. Hirvonen, Atmospheric pressure plasma enhanced chemical vapor deposition of hydrophobic coatings using fluorine-based liquid precursors, *Surf. Coatings Technol.* 234 (2013).
- [5] D.J. Marchand, Z.R. Dilworth, R.J. Stauffer, E. Hsiao, J.H. Kim, J.G. Kang, S.H. Kim, Atmospheric rf plasma deposition of superhydrophobic coatings using tetramethylsilane precursor, *Surf. Coatings Technol.* 234 (2013) 14–20.
- [6] A. Ladwig, S. Babayan, M. Smith, M. Hester, W. Highland, R. Koch, R. Hicks, Atmospheric plasma deposition of glass coatings on aluminum, *Surf. Coatings Technol.* 201 (2007) 6460–6464.
- [7] A. Vogelsang, A. Ohl, R. Foest, K. Schröder, K.-D. Weltmann, Hydrophobic coatings deposited with an atmospheric pressure microplasma jet, *J. Phys. D. Appl. Phys.* 43 (2010) 485201.
- [8] R.E. Johnson, R.H. Dettre, Contact Angle Hysteresis. III. Study of an Idealized Heterogeneous Surface, *J. Phys. Chem.* 68 (1964) 1744–1750.
- [9] W. Barthlott, C. Neinhuis, Purity of the sacred lotus, or escape from contamination in biological surfaces, *Planta*. 202 (1997) 1–8.
- [10] A. Lafuma, D. Quéré, Superhydrophobic states, *Nat. Mater.* 2 (2003) 457–460.
- [11] H.K. Raut, V.A. Ganesh, A.S. Nair, S. Ramakrishna, Anti-reflective coatings: A critical, in-depth review, *Energy Environ. Sci.* 4 (2011) 3779.
- [12] S. Farhadi, M. Farzaneh, S.A. Kulinich, Anti-icing performance of superhydrophobic surfaces, *Appl. Surf. Sci.* 257 (2011) 6264–6269.
- [13] S. Chattopadhyay, Y.F. Huang, Y.J. Jen, A. Ganguly, K.H. Chen, L.C. Chen, Anti-reflecting and photonic nanostructures, *Mater. Sci. Eng. R Reports.* 69 (2010) 1–35.
- [14] C.-H. Xue, S.-T. Jia, J. Zhang, L.-Q. Tian, H.-Z. Chen, M. Wang, Preparation of superhydrophobic surfaces on cotton textiles, *Sci. Technol. Adv. Mater.* 9 (2008) 035008.
- [15] X. Zhang, F. Shi, J. Niu, Y. Jiang, Z. Wang, Superhydrophobic surfaces: from structural control to functional application, *J. Mater. Chem.* 18 (2008) 621–633.
- [16] J. Genzer, K. Efimenko, Recent developments in superhydrophobic surfaces and their relevance to marine fouling: A review, *Biofouling*. 22 (2006) 339–360.
- [17] M. Masuko, H. Miyamoto, A. Suzuki, Shear strength and durability of self assembled monolayer,

- 2007 Proc. ASME/STLE Int. Jt. Tribol. Conf. IJTC 2007. PART A (2008) 3–5.
- [18] I. Topala, M. Asandulesa, D. Spridon, N. Dumitrascu, Hydrophobic coatings obtained in atmospheric pressure plasma, *IEEE Trans. Plasma Sci.* 37 (2009) 946–950.
- [19] M.T. Laugier, An energy approach to the adhesion of coatings using the scratch test, *Thin Solid Films.* (1984).
- [20] J. Valli, U. Mäkelä, A. Matthews, V. Murawa, TiN coating adhesion studies using the scratch test method, *J. Vac. Sci. Technol. A Vacuum, Surfaces, Film.* (1985).
- [21] V.D. Jardret, W.C. Oliver, On the robustness of scratch testing for thin films: The issue of tip geometry for critical load measurement, in: *Thin Film. Mech. Prop.* Viii, 2000.
- [22] A.J. Perry, The adhesion of chemically vapour-deposited hard coatings to steel-the scratch test, *Thin Solid Films.* (1981).
- [23] R.L. Browning, G.T. Lim, A. Moyse, H.J. Sue, H. Chen, J.D. Earls, Quantitative evaluation of scratch resistance of polymeric coatings based on a standardized progressive load scratch test, *Surf. Coatings Technol.* (2006).
- [24] S.J. Bull, E. G.-Berasetegui, Chapter 7 An overview of the potential of quantitative coating adhesion measurement by scratch testing, *Tribol. Interface Eng. Ser.* (2006).
- [25] P.A. Steinmann, Y. Tardy, H.E. Hintermann, Adhesion testing by the scratch test method: The influence of intrinsic and extrinsic parameters on the critical load, *Thin Solid Films.* (1987).
- [26] J. Valli, U. Mäkelä, Applications of the scratch test method for coating adhesion assessment, *Wear.* (1987).
- [27] ASTM (American Society for Testing and Materials), D7027 - Standard Test Method for Evaluation of Scratch Resistance of Polymeric Coatings and Plastics Using an Instrumented Scratch Machine, *ASTM Int.* (2013).
- [28] P. Richard, J. Thomas, D. Landolt, G. Gremaud, Combination of scratch-test and acoustic microscopy imaging for the study of coating adhesion, *Surf. Coatings Technol.* (1997).
- [29] R.S.R. Kalidindi, R. Subasri, Sol-gel nanocomposite hard coatings, in: *Anti-Abrasive Nanocoatings Curr. Futur. Appl.*, 2014.
- [30] L. Kilpi, O.M.E. Yliivaara, A. Vaajoki, J. Malm, S. Sintonen, M. Tuominen, R.L. Puurunen, H. Ronkainen, Microscratch testing method for systematic evaluation of the adhesion of atomic layer deposited thin films on silicon, *J. Vac. Sci. Technol. A Vacuum, Surfaces, Film.* 34 (2016) 01A124.
- [31] Q.H. Trinh, S.B. Lee, Y.S. Mok, Hydrophobic Coating of Silicate Phosphor Powder Using Atmospheric Pressure Dielectric Barrier Discharge Plasma, *Am. Inst. Chem. Eng.* 60 (2014) 829–838.
- [32] S. Sportouch, C. Lacoste, R. Gaufrés, Spectres Raman du néopentane et du tétraméthylsilane à l'état gazeux, *J. Mol. Struct.* 9 (1971) 119–127.
- [33] N. Herlin, M. Lefebvre, M. Pealat, J. Perrin, Investigation of the Chemical Vapor Deposition of Silicon Carbide from Tetramethylsilane by in Situ Temperature and Gas Composition Measurements, *J. Phys. Chem.* 96 (1992) 7063–7072.

- [34] D. Ball, T. Carter, D. McKean, L. Woodward, Raman and infra-red spectra of methyl silane and some deuterated derivatives, *Spectrochim. Acta.* 20 (1964) 1721.
- [35] M. Gueye, T. Gries, C. Noël, S. Migot-Choux, S. Bulou, E. Lecoq, P. Choquet, K. Kutasi, T. Belmonte, Interaction of (3-Aminopropyl)triethoxysilane with Pulsed Ar–O<sub>2</sub> Afterglow: Application to Nanoparticles Synthesis, *Plasma Chem. Plasma Process.* 36 (2016) 1031–1050.
- [36] V.R. Rai, S. Agarwal, Mechanism of self-catalytic atomic layer deposition of silicon dioxide using 3-aminopropyl triethoxysilane, water, and ozone, *Chem. Mater.* 23 (2011) 2312–2316.
- [37] P.J. Launer, Infrared Absorption Bands Characteristic of the Si-CH<sub>2</sub>CH<sub>2</sub>CN and Si-CH<sub>2</sub>CH<sub>2</sub>CH<sub>2</sub>CN Groups, *Silicon Compd. Regist. Rev.* (1987) 100–103.
- [38] I.A. Rahman, M. Jafarzadeh, C.S. Sipaut, Synthesis of organo-functionalized nanosilica via a co-condensation modification using  $\gamma$ -aminopropyltriethoxysilane (APTES), *Ceram. Int.* 35 (2009) 1883–1888.
- [39] H. Okabayashi, I. Shimizu, E. Nishio, C.J. O'Connor, Diffuse reflectance infrared Fourier transform spectral study of the interaction of 3-aminopropyltriethoxysilane on silica gel. Behavior of amino groups on the surface, *Colloid Polym. Sci.* 275 (1997) 744–753.
- [40] L.D. White, C.P. Tripp, Reaction of (3-Aminopropyl)dimethylethoxysilane with Amine Catalysts on Silica Surfaces, *J. Colloid Interface Sci.* 232 (2000) 400–407.
- [41] J.N. Borges, T. Belmonte, J. Guillot, D. Duday, M. Moreno-Couranjou, P. Choquet, H.N. Migeon, Functionalization of copper surfaces by plasma treatments to improve adhesion of epoxy resins, in: *Plasma Process. Polym.*, 2009.
- [42] V. Gubala, R.P. Gandhiraman, C. Volcke, C. Doyle, C. Coyle, B. James, S. Daniels, D.E. Williams, Functionalization of cycloolefin polymer surfaces by plasma-enhanced chemical vapour deposition: comprehensive characterization and analysis of the contact surface and the bulk of aminosiloxane coatings, *Analyst.* 135 (2010) 1375–1381.
- [43] C. Volcke, R.P. Gandhiraman, V. Gubala, C. Doyle, G. Fonder, P.A. Thiry, A.A. Cafolla, B. James, D.E. Williams, Plasma functionalization of AFM tips for measurement of chemical interactions, *J. Colloid Interface Sci.* 348 (2010) 322–328.
- [44] C. Volcke, R.P. Gandhiraman, V. Gubala, J. Raj, T. Cummins, G. Fonder, R.I. Nooney, Z. Mekhalif, G. Herzog, S. Daniels, D.W.M. Arrigan, A.A. Cafolla, D.E. Williams, Reactive amine surfaces for biosensor applications, prepared by plasma-enhanced chemical vapour modification of polyolefin materials, *Biosens. Bioelectron.* 25 (2010) 1875–1880.
- [45] W. Juda, Preparation of Ion Exchange Membranes, *J. Appl. Polym. Sci.* 5193 (1953) 875–884.
- [46] Y. Liu, Y. Li, X.M. Li, T. He, Kinetics of (3-aminopropyl)triethoxysilane (APTES) silanization of superparamagnetic iron oxide nanoparticles, *Langmuir.* 29 (2013) 15275–15282.
- [47] J.A. Howarter, J.P. Youngblood, Surface modification of polymers with 3-aminopropyltriethoxysilane as a general pretreatment for controlled wettability, *Macromolecules.* 40 (2007) 1128–1132.
- [48] C.L. Loch, D. Ahn, Chen, J. Wang, Z. Chen, Sum Frequency Generation Studies at Poly(ethylene terephthalate)/Silane Interfaces: Hydrogen Bond Formation and Molecular Conformation Determination, *Langmuir.* 20 (2004) 5467–5473.

- [49] J.H. Yim, V. Rodriguez-Santiago, A.A. Williams, T. Gougousi, D.D. Pappas, J.K. Hirvonen, Atmospheric pressure plasma enhanced chemical vapor deposition of hydrophobic coatings using fluorine-based liquid precursors, *Surf. Coatings Technol.* 234 (2013) 21–32.
- [50] F. Alba-Elías, J. Ordieres-Meré, A. González-Marcos, Deposition of thin-films on EPDM substrate with a plasma-polymerized coating, *Surf. Coatings Technol.* 206 (2011) 234–242.
- [51] J. Schäfer, R. Foest, A. Quade, A. Ohl, J. Meichsner, K.D. Weltmann, Carbon-free SiO<sub>x</sub> films deposited from octamethylcyclotetrasiloxane (OMCTS) by an atmospheric pressure plasma jet (APPJ), *Eur. Phys. J. D.* 54 (2009) 211–217.
- [52] T.J. Lin, J.A. Antonelli, D.J. Yang, H.K. Yasuda, F.T. Wang, Plasma treatment of automotive steel for corrosion protection - a dry energetic process for coatings, *Prog. Org. Coatings.* 31 (1997) 351–361.
- [53] K.T.L. Trinh, H. Zhang, D.J. Kang, S.H. Kahng, B.D. Tall, N.Y. Lee, Fabrication of polymerase chain reaction plastic Lab-on-a-Chip device for rapid molecular diagnoses, *Int. Neurourol. J.* 20 (2016) S38–S48.
- [54] V.M. Gun'ko, O. Seledets, J. Skubiszewska-Zięba, V.I. Zarko, R. Lebeda, W. Janusz, S. Chibowski, Phosphorus-containing carbon deposits on silica gel Si-100, *Microporous Mesoporous Mater.* 87 (2005) 133–145.
- [55] C.-W. Kan, C.-H. Kwong, S.-P. Ng, Atmospheric Pressure Plasma Surface Treatment of Rayon Flock Synthetic Leather with Tetramethylsilane, *Appl. Sci.* 6 (2016) 59.
- [56] Y. Li, J. Zhang, S. Zhu, H. Dong, F. Jia, Z. Wang, Z. Sun, L. Zhang, Y. Li, H. Li, W. Xu, B. Yang, Biomimetic surfaces for high-performance optics, *Adv. Mater.* 21 (2009) 4731–4734.

Table 1. Thickness and RMS roughness of each sample

Sample	Thickness (nm)	RMS roughness (nm)
APTES	103	$37 \pm 5$
TMS/APTES = 3	218	$64 \pm 4$
TMS/APTES = 3.4	270	$71 \pm 7$
TMS/APTES = 3.7	300	$85 \pm 7$
TMS/APTES = 4.8	431	$108 \pm 5$
TMS/APTES = 6	480	$117 \pm 5$
TMS	460	$120 \pm 5$

Table 2. Deconvolution of C1s spectra along with binding energies and functional groups

Functional groups	Peak Position (eV)	References
C-C, C-H	~284.7	[3,55]
C-O, C-N	~286	[3,55]
C=O	~287.5	[3,55]
O-C-O	~288.7	[3,55]

Table 3. Scratch test results (breakdown force)

Sample	Annealing temperature (°C)	Coating thickness (nm)	Treatment time (min)	Deposition rate* (nm/min)	Applied force (dyne)
APTES only	250	400	16.5	25.9	16671
TMS/APTES=3	250	400	8.3	56.2	14709
TMS/APTES=3.4	250	400	7.1	64.5	10767
TMS/APTES=3.7	250	400	6.1	85.5	9316
TMS/APTES=4.8	250	400	4.2	67.8	7354
TMS/APTES=6	250	400	4.1	86.2	3432
TMS only	250	400	6.4	64.5	3432

\*This is the slope value of linear fitting

**Figure captions**

Figure 1. The schematic figure of the experimental setup (a) and custom-built scratch tester (b).

Figure 2. Discharge photograph image of the plasma jet.

Figure 3. Dependence of WCA on (a) treatment time, (b) applied voltage, (c) the TMS/APTES ratio and (d) the flow rate of the carrier gas (d).

Figure 4. Photograph image of the coated surface in the coated state.

Figure 5. (a) Effect of aging time and (b) annealing temperature on the coating.

Figure 6. AFM images of the coated samples. [TM = TMS and AP = APTES, (a) APTES only, (b) TM/AP = 3, (c) TM/AP = 3.4, (d) TM/AP = 3.7, (e) TM/AP = 4.8, (f) TM/AP = 6, (g) TMS only]

Figure 7. SEM images of the coated samples. [TM = TMS and AP = APTES, (a) APTES only, (b) TM/AP = 3, (c) TM/AP = 3.4, (d) TM/AP = 3.7, (e) TM/AP = 4.8, (f) TM/AP = 6, (g) TMS only]

Figure 8. (a) Gas-phase FTIR spectra of the Ar/TMS without (black) and with (red) plasma and (b) gas-phase FTIR spectra of the Ar/APTES without (black) and with (red) plasma from 1000 to 3500  $\text{cm}^{-1}$ .

Figure 9. Possible reaction routes and mechanism of APTES for the surface modification: (a) hydrogen bonding due to initial adsorption, (b) surface attachment, and (c) multilayer formation.

Figure 10. FTIR spectra of coated samples from 500 to 4000  $\text{cm}^{-1}$ .

Figure 11. Elemental composition (%) of sample surfaces.

Figure 12. Deconvolution of C1s spectra (282–290 eV) of the coated samples.

Figure 13. UV-Vis transmission of the coated samples.

Figure 14. Scratch test results sustained by the samples.

### Highlights

- Robust coating on the glass by APPJ conjugated with two precursors
- Coating strength depended on the flow rate, voltage, time and TMS/APTES ratio
- The coating exhibited good durability, mechanical strength and thermal stability

ACCEPTED MANUSCRIPT

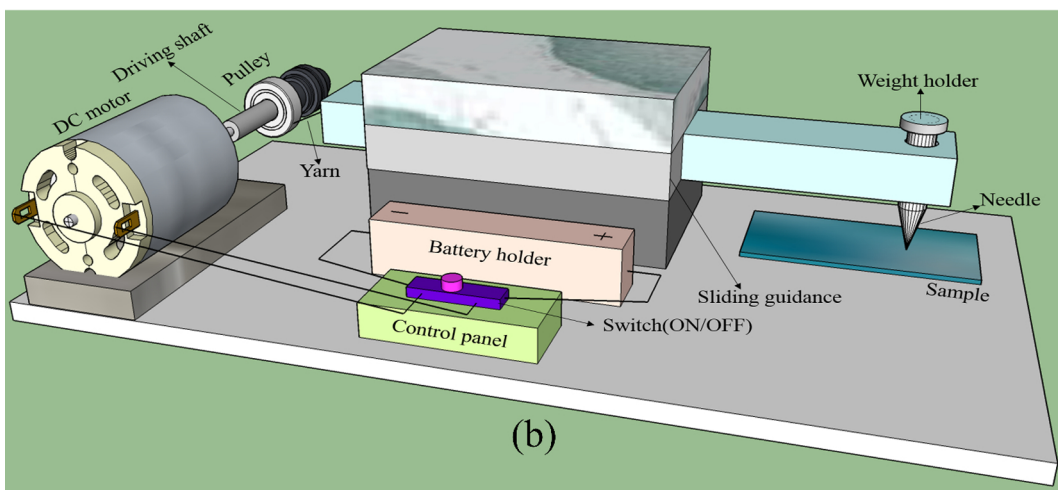
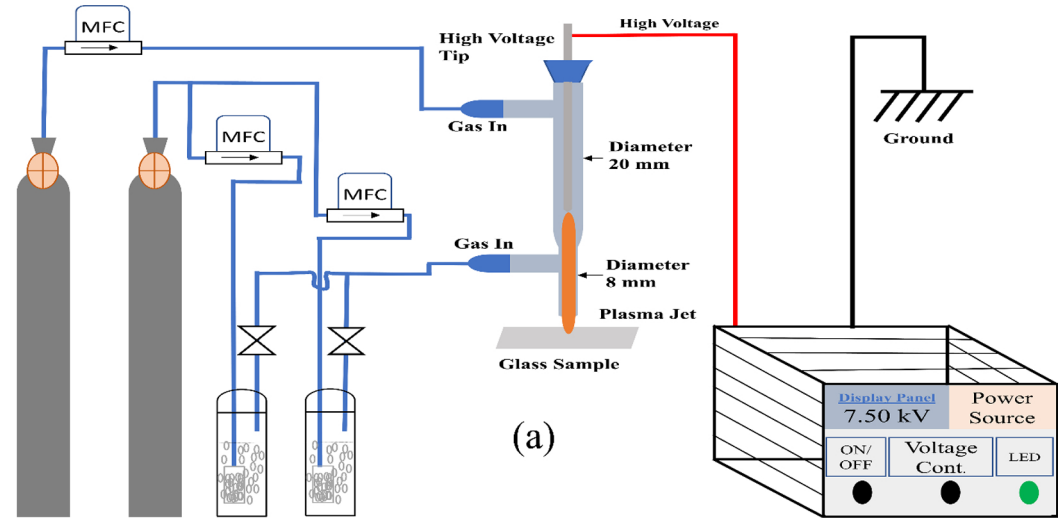


Figure 1

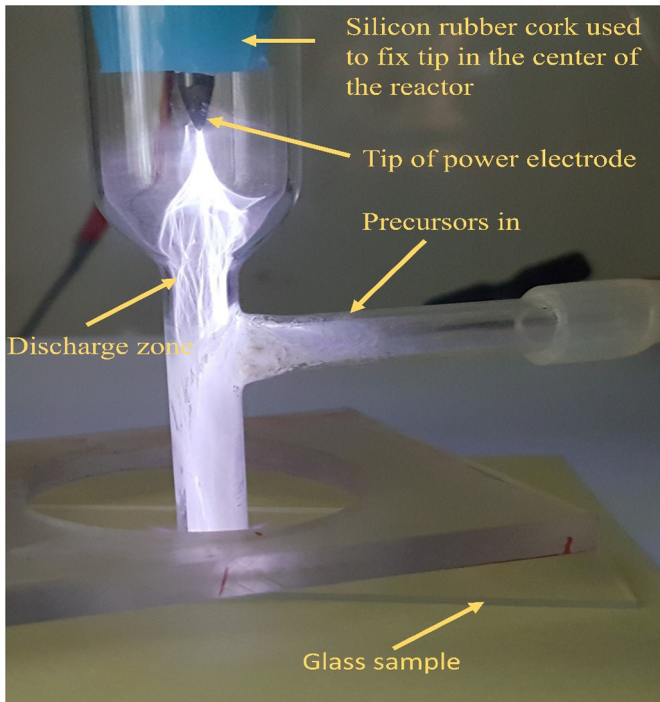


Figure 2

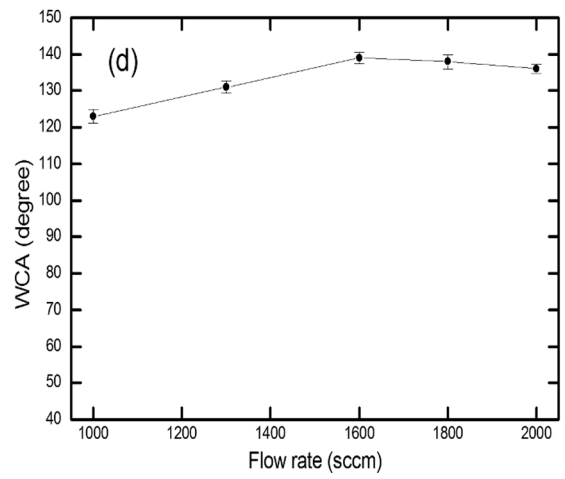
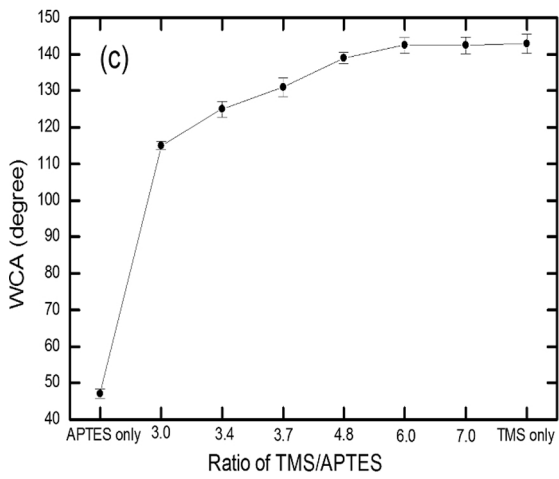
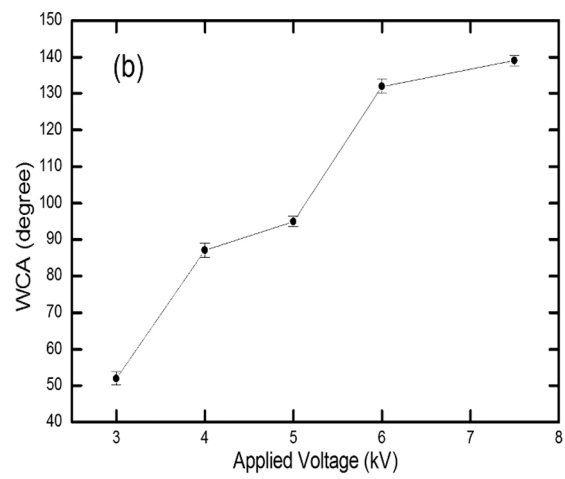
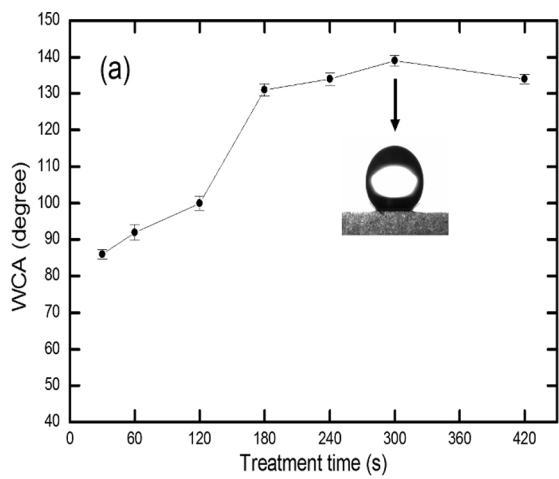
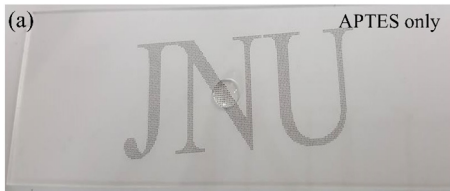


Figure 3

Top view



Side view

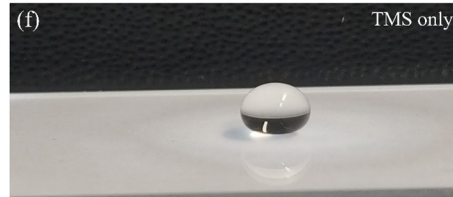
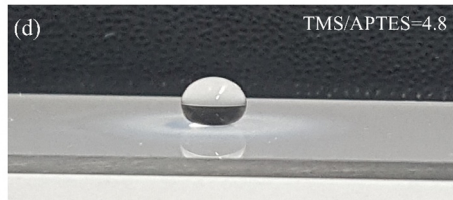
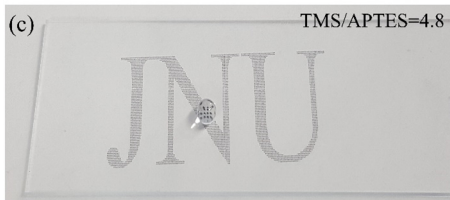


Figure 4

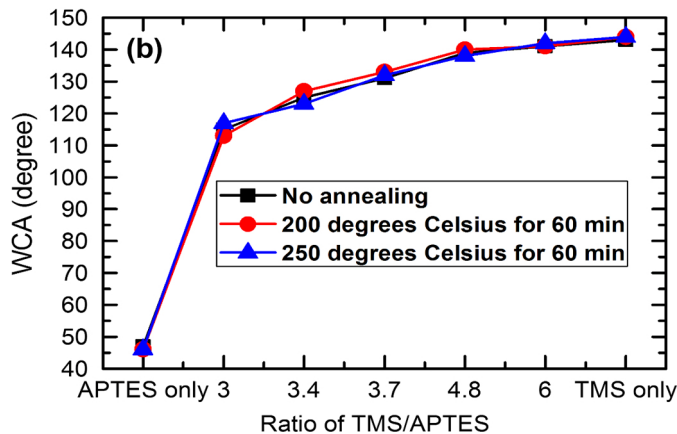
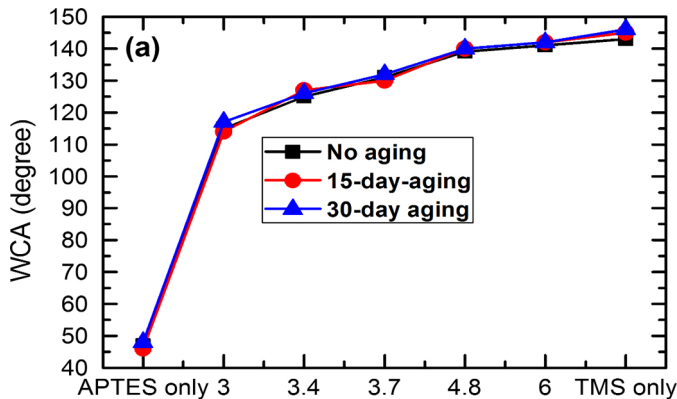


Figure 5

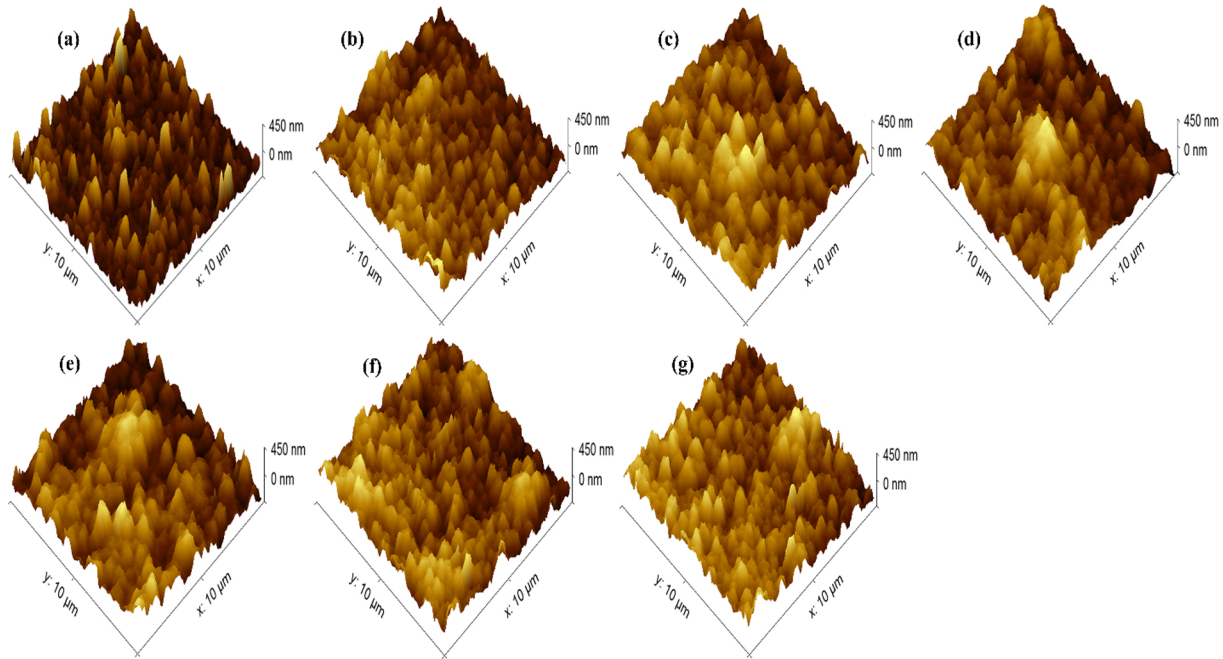


Figure 6

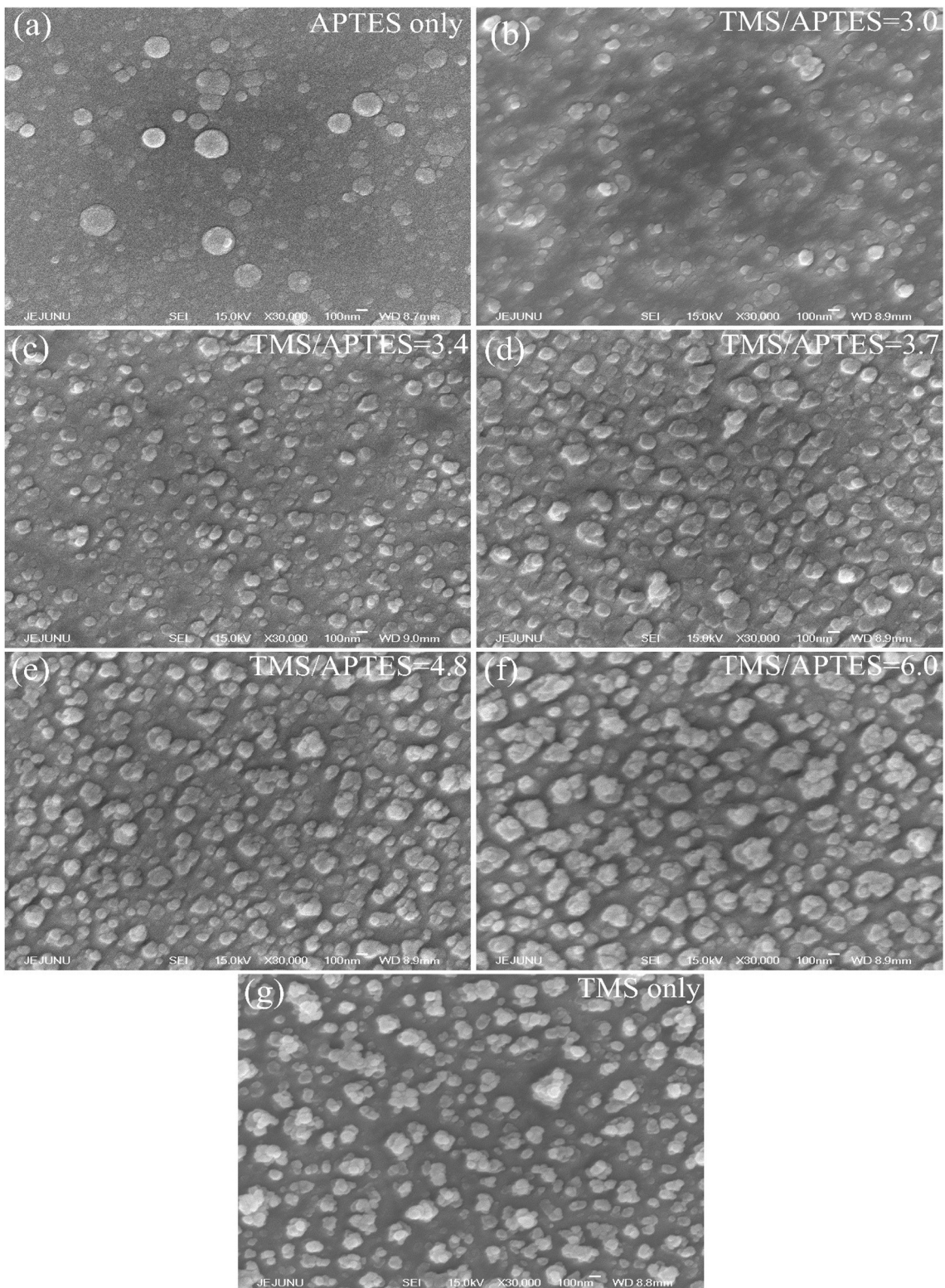


Figure 7

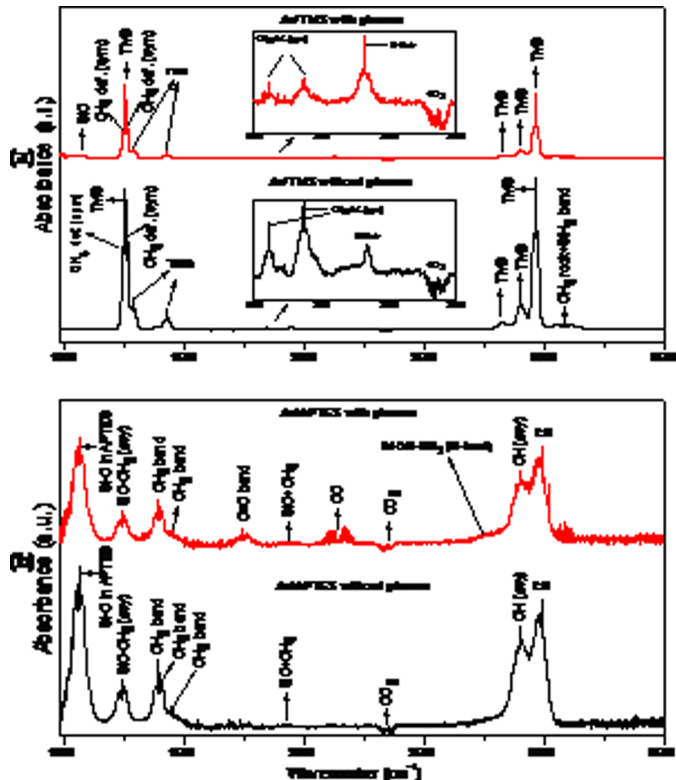


Figure 8

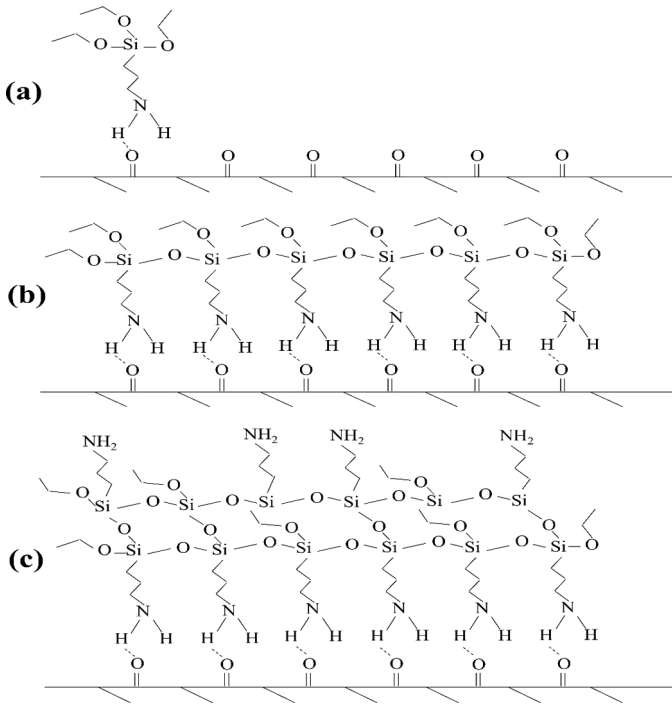


Figure 9

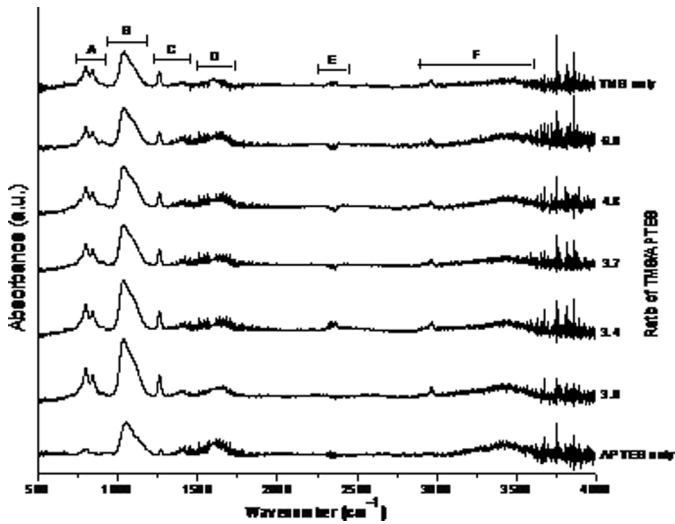


Figure 10

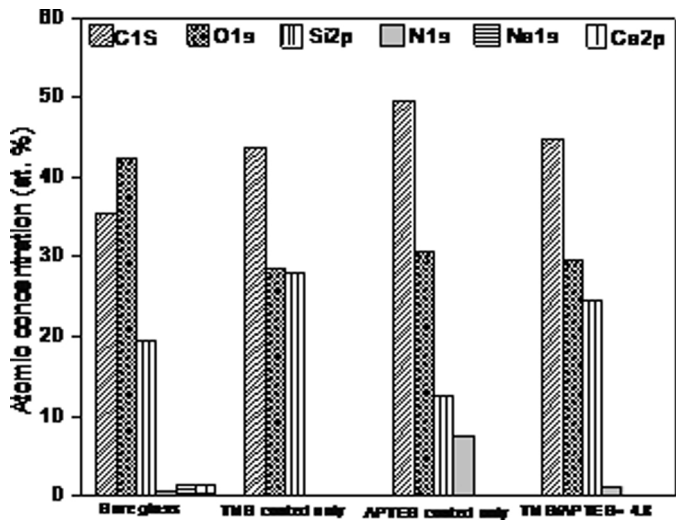


Figure 11

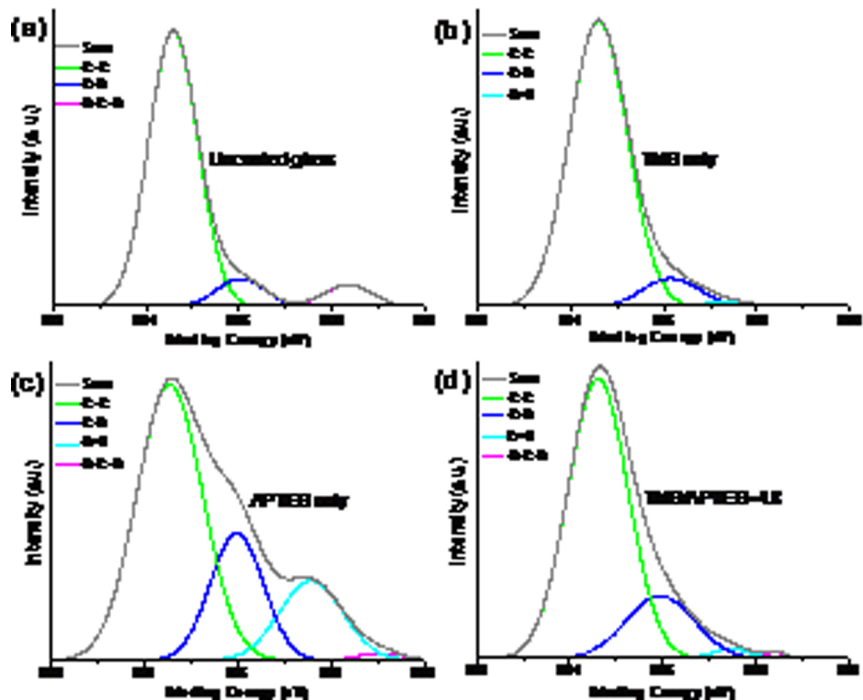


Figure 12

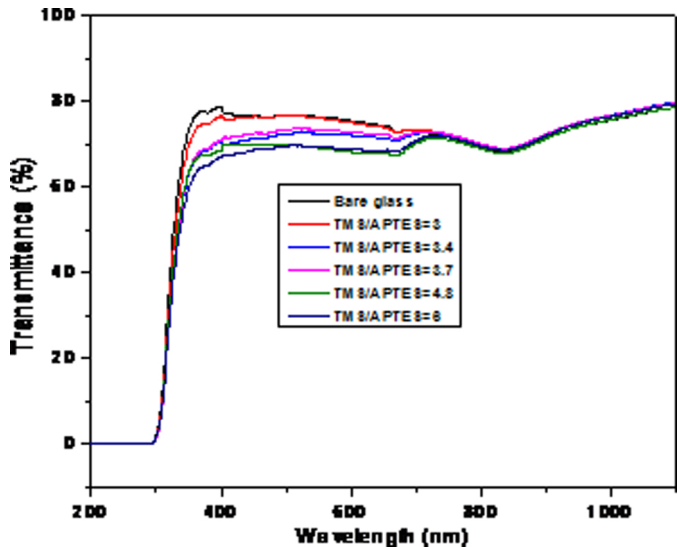


Figure 13

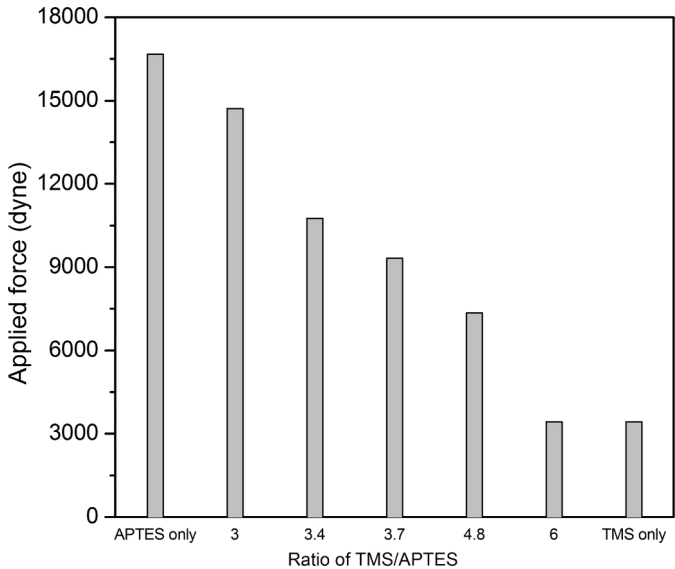


Figure 14